

ARTICLE OPEN



Degradation of ancient Maya carved tuff stone at Copan and its bacterial bioconservation

Kerstin Elert¹, Encarnación Ruiz-Agudo¹, Fadwa Jroundi², Maria Teresa Gonzalez-Muñoz², Barbara W. Fash³, William L. Fash⁴, Nieves Valentin⁵, Alberto de Tagle⁶ and Carlos Rodriguez-Navarro¹✉

Much stone sculptural and architectural heritage is crumbling, especially in intense tropical environments. This is exemplified by significant losses on carvings made of tuff stone at the Classic Maya site of Copan. Here we demonstrate that Copan stone primarily decays due to stress generated by humidity-related clay swelling resulting in spalling and material loss, a damaging process that appears to be facilitated by the microbial bioweathering of the tuff stone minerals (particularly feldspars). Such a weathering process is not prevented by traditional polymer- and alkoxy silane-based consolidants applied in the past. As an alternative to such unsuccessful conservation treatments, we prove the effectiveness of a bioconservation treatment based on the application of a sterile nutritional solution that selectively activates the stone's indigenous bacteria able to produce CaCO₃ biocement. The treatment generates a bond with the original matrix to significantly strengthen areas of loss, while unexpectedly, bacterial exopolymeric substances (EPS) impart hydrophobicity and reduce clay swelling. This environmentally-friendly bioconservation treatment is able to effectively and safely preserve fragile stones in tropical conditions, opening the possibility for its widespread application in the Maya area, and elsewhere.

npj Materials Degradation (2021)5:44; <https://doi.org/10.1038/s41529-021-00191-4>

INTRODUCTION

Deterioration of stone results in the loss of invaluable pieces of sculptural and architectural heritage¹. Damage is particularly dramatic in hot and humid environments such as the Maya area in Mesoamerica, where archaeological sites, excavated structures, and inscribed stone monuments are exposed to heavy rainfall and high humidity and temperature conditions that exacerbate physical and chemical weathering, as well as biodeterioration^{2,3}. Different conservation materials, such as polymers or alkoxy silanes have been applied as protectives and/or consolidants to halt or minimize the deleterious effects of such weathering processes^{1,4}. So far, however, most treatments had either limited success¹, or even exacerbated damage⁵.

These problems are exemplified by the case of the archaeological site of Copan (Supplementary Fig. 1), one of the most remarkable Classic Maya (250–900 CE) centers in Mesoamerica and designated a UNESCO World Heritage Site⁶. Copan was built using a local volcanic tuff⁷. After extensive archaeological excavation starting at the end of the 19th c and the first half of the 20th c, reliefs of inscribed stone blocks (hieroglyphs), architectural sculptures, and stelae started to degrade at a rapid pace. Figure 1a–d shows pictures of the Hieroglyphic Stairway of Copan (dedicated 756 CE), the longest known Maya inscription, taken in 1895 and in 2004. Massive loss of stone material rendered parts of the hieroglyphs almost unreadable. Remarkably, some carved blocks adjacent to damaged ones are in a good state of conservation (Fig. 1d and Supplementary Fig. 1e). Since the 1950s, studies performed to understand the decay process generally concluded that biodeterioration was the main culprit^{8,9}. As a result, biocide treatments were massively applied since the 1970s without any positive effect⁸. The presence of clays in the tuff stone was considered as a factor in its deterioration⁸, but neither a

definitive proof for such a link has been presented, nor an effective conservation treatment for such a potential weathering mechanism was developed. Consolidation with acrylic polymers and alkoxy silanes was implemented in the 1980s and 1990s, but proved ineffective in the long-term^{8,9}.

To gather detailed information on the degradation mechanism (s) of Copan stone as a basis for its conservation, here we sampled different stone blocks at Copan (Supplementary Fig. 1), and analyzed their chemical and textural features. Subsequently, we tested on a clay-rich volcanic tuff stone and under the site's tropical environment, an advanced bioconservation treatment we have developed that is based on the bacterial biomineralization of calcium carbonate following the application of a sterile nutritional solution (M-3P; see Methods) that selectively activates the stone's indigenous carbonatogenic bacteria. This alternative ecological bioconservation approach exploits the capacity of several bacteria of producing CaCO₃ via different metabolic routes, a process that is ubiquitous in nature¹⁰. The main advantage of our method is the fact that it does not require the isolation, culture, and application of a carbonatogenic bacteria inoculum to the stone artwork¹¹ as occurs in the case of previous bacterial conservation methods^{10,12}. Our method is thus more economic and easier to apply, especially in locations with difficult accessibility, such as the Maya area, and has shown very promising results when applied on limestones in several monuments in southern Europe^{13–15}. Here, we applied the sterile M-3P solution both in situ, on selected trial areas in the north wall of Structure 10L-18 (Fig. 1e) showing extensive damage and loss of surface material (Fig. 1f), as well as ex situ, in the laboratory, on tuff stone blocks collected from different areas of the Copan Acropolis. The application of our biomineralization treatment on Copan tuff stone represents a unique possibility to test the efficacy of this method is an intense

¹Department of Mineralogy and Petrology, University of Granada, Granada, Spain. ²Department of Microbiology, University of Granada, Granada, Spain. ³Peabody Museum, Harvard University, Cambridge, MA, USA. ⁴Department of Anthropology, Harvard University, Cambridge, MA, USA. ⁵Conservation consultant, Madrid, Spain. ⁶Conservation consultant, Cos, Cantabria, Spain. ✉email: carlosrn@ugr.es

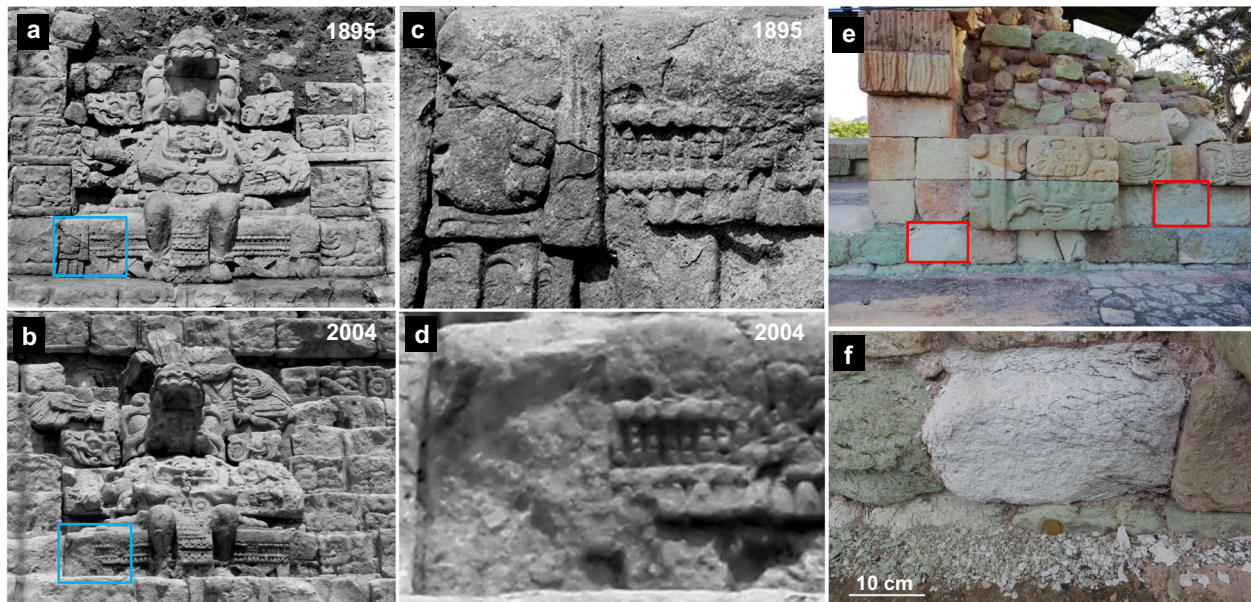


Fig. 1 Decay of Maya tuff stone at Copan. Images of the first seated ruler portrait in the Hieroglyphic Stairway taken after partial reconstruction in 1895 (a) and in 2004 (b). Significant surface stone material has been lost leading to the disappearance of relief details as shown by the high magnification image pairs (c, d) corresponding to the blue squares in (a) and (b); (e) general view of the area of Structure 10L-18 selected for the field trial application of the bacterial bioconsolidation treatment. The red-squared blocks were treated with the M-3P solution; (f) detail of the decay suffered by the tuff stone blocks, resulting in massive flaking and scaling, and the accumulation of stone debris at the bottom of the wall in Structure 10L-18. Credits: (a) Courtesy of the Peabody Museum of Archaeology and Ethnology, Harvard University, PM 2004.24.1865.1; (b) Image by Barbara W. Fash.

tropical environmental and on an exceptionally challenging non-carbonate stone substrate containing clays. The evaluation of the physical-mechanical and mineralogical-textural features of the treated stones, as well as the evolution of the stone microbiota shows that this treatment is highly effective. Moreover, no undesired side effects were observed during the period of evaluation. We anticipate that the treatment could be effectively deployed in the Maya area, where there is a strong need and demand for effective conservation treatments. It could also be effective in other tropical locations and elsewhere, particularly in the case of clay-containing stones for which there is no fully effective conservation treatment so far^{16–22}.

RESULTS AND DISCUSSION

Characterization of Copan tuff stone

Copan tuff composition ranges from trachydacite to rhyodacite (Supplementary Table 1 and Supplementary Fig. 2). Under the petrographic microscope it shows a volcanoclastic rock texture, with a partially devitrified glass matrix and scattered micro-to-millimeter sized feldspars, quartz, and scarce biotite phenocrysts, along with sparse mm-sized lithoclasts (basalt) (Fig. 2a). Stone blocks showing a high degree of alteration systematically display pervasive fractures parallel to the exposed surface (Fig. 2a). The separation among parallel fractures is ~0.5–3 mm, which matches the thickness of scales falling off the stone blocks and carved surfaces at Copan. The stone porosity is moderate to high, according to water saturation under vacuum ($27 \pm 3\%$, $N=4$) and mercury intrusion porosimetry (MIP) ($28 \pm 2\%$, $N=2$) analyses. Note that the average porosity values correspond to the different Copan tuff stone varieties defined below. X-ray diffraction (XRD) analysis of powder samples (Fig. 2b) and oriented aggregates (Fig. 2c) enabled us to define three main tuff lithotypes: Type 1 includes abundant kaolinite and quartz, with small amounts of albite and sanidine (Supplementary Figs. 3 and 4). It is buff-colored and shows minimal decay; Type 2

corresponds to the most abundant whitish/buff or greenish-colored stones, commonly displaying scaling and flaking. It contains smectites (montmorillonite) along with zeolites (mordenite, either alone or with heulandite and/or clinoptilolite), in addition to quartz, sanidine, and albite (Fig. 2b, c and Supplementary Fig. 4); and Type 3 corresponds to green colored, highly deteriorated stone blocks showing massive scaling and flaking. It includes abundant smectites and the zeolite analcime, along with quartz and feldspars. Quantitative XRD Rietveld analysis showed that Copan stone contained up to ~9 wt% smectites and 12–33 wt% glass (amorphous) fraction (Supplementary Fig. 4). In a few samples, especially those collected close to modern cement mortars, gypsum (≤ 5 wt%) and trace amounts of calcite were detected.

Field emission scanning electron microscopy (FESEM) with X-ray spectrometry (EDS) microanalysis shows abundant kaolinite in Type 1 stones (Supplementary Fig. 3) and micro- to nanometer-sized flake-like smectite and prism-shaped zeolite crystals in the porous matrix of Type 2 and 3 stones, surrounding larger quartz and feldspar phenocrysts (Fig. 2d). Some feldspars showed corrosion features in association with microbial biofilms (Supplementary Fig. 5), as observed after microbial bioweathering²³. Transmission electron microscopy (TEM) and high-angle annular dark-field (HAADF) imaging, along with EDS analyses show that the smectite in Type 2 and 3 tuffs is montmorillonite (Fig. 2e) with the representative structural formula $K_{0.07}Ca_{0.27}Mg_{0.21}Fe_{0.43}Al_{1.47}Si_{3.81}O_{10}(OH)_2$.

These analyses confirm that this tuff underwent hydrothermal alteration to different extents leading to zeolitization and formation of clay minerals, including smectites^{7,17}, explaining the differences among the three lithotypes identified here. Such intrinsic compositional differences appear to be at the root of the differential weathering observed on-site (Fig. 1 and Supplementary Fig. 1e). This suggests that chemical weathering and/or biodeterioration are not the main causes of decay. Otherwise, all stone blocks exposed to similar conditions should display a more or less comparable level of decay.

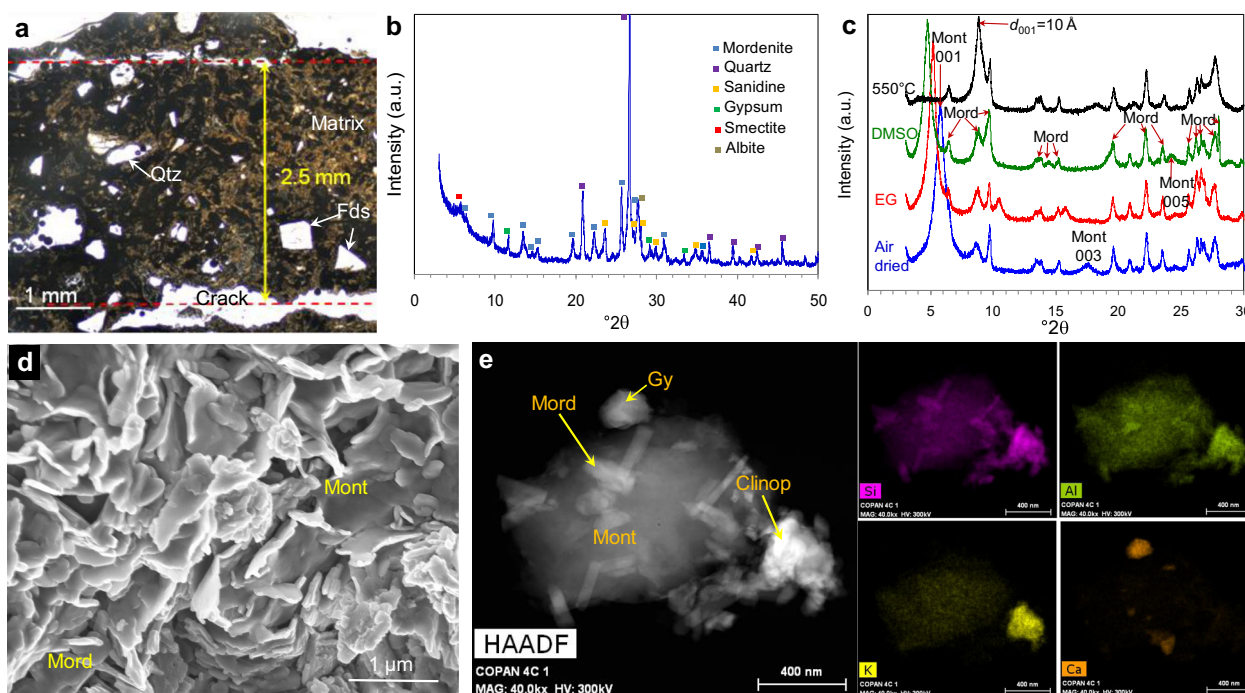


Fig. 2 **Texture and mineralogy of Copan stone.** **a** Optical microscopy image of the partially devitrified glass matrix with scattered quartz (Qtz) and feldspar (Fds) phenocrystals (plane light). Note the development of fractures parallel to the stone surface (upper part) with separation of ~ 2.5 mm. **b** XRD pattern of representative greenish-colored tuff stone (Copan 3). **c** XRD pattern of oriented aggregates of the clay fraction. Note the shifting to lower 2θ angles after solvation with EG and DMSO, and the collapse of the montmorillonite (Mont) main Bragg peak from $d_{001} = 14.9$ Å to $d_{001} = 10$ Å after heat treatment. Note also that mordenite (Mord) is an abundant phase in the fraction < 2 μm . **d** FESEM image of montmorillonite (flake-like) particles along with mordenite (prism-like) particles. **e** HAADF STEM image and corresponding elemental maps of the main phases present in the devitrified matrix of the most abundant buff or greenish colored tuff (Copan stone Type 2), made up of montmorillonite, mordenite, and clinoptilolite (Clinop), along with traces of gypsum (Gy).

Decay mechanism of Copan stone

Considering that swelling clays (smectites) were a substantial component of the stone types most prone to decay, a hydric expansion test was performed (see Methods). Free swelling strain (ϵ) values of Type 2 (Fig. 3a; $\epsilon = 0.0039 \pm 0.0007$; $N = 6$) and Type 3 (up to $\epsilon = 0.005$) are at the upper end of those reported for tuff stones containing swelling clays²⁰. Notably, after each wetting-drying cycle an incremental residual strain was detected ($\epsilon_{\text{res}} = 0.0018 \pm 0.0007$; $N = 5$), indicating a permanent deformation due to crack formation. The kinetics of water absorption was faster than the associated swelling strain due to a time delay for the development of hydric expansion, which typically displayed sudden jumps, likely corresponding to cracks opening (Fig. 3b). A smaller expansion ($\epsilon = 0.00053 \pm 0.00035$, $N = 7$) was observed in Type 1 stone (with non-swelling kaolinite) and in a few Type 2 stone samples with an unusually low smectite content (≤ 2 wt%), which showed a low level of decay. In these cases, no residual strain was observed after wet-dry cycling. Figure 3c shows the clear correlation between smectite content and ϵ of Copan stone. The good exponential fitting (instead of the expected linear relationship) is likely due to the non-zero strain observed in smectite-free stones, which also occurs in a range of crystalline rocks due to solvation forces²⁴. Such low strain values are below the commonly reported threshold of 0.0015 for damage generation upon clay expansion¹⁸.

In situ micro X-ray computed tomography (μ -CT) imaging (Fig. 3d–f) showed an increase in the total porosity from $14 \pm 2\%$ (dry stone) up to $17 \pm 2\%$ after water flooding (note that because pores < 4.7 μm in size cannot be resolved under our μ -CT experimental conditions, the total porosity was lower than that determined by water saturation or MIP). In parallel, a reduction of the non-connected fraction of pores from 20% to 17% was observed.

These results are consistent with crack formation and propagation (connecting non-connected pores and increasing the total porosity of the stone).

Clay swelling/shrinking upon wet-dry cycling is recognized as one of the main mechanisms of physical weathering of stone^{16,18,20}. Clay expansion occurs by: (i) non-continuous intracrystalline swelling, involving the incorporation of successive water monolayers into the (001) interlayer of swelling clays and resulting in discrete increases in d_{001} -spacing; and (ii) continuous osmotic swelling resulting from differences in ionic activity between clay particles (high) and the bulk solution (low), leading to water ingress between nearby clay particles¹⁶. Both processes create swelling stress, being the first one the main contributor¹⁹. In some cases, such swelling stress overcomes the critical stress intensity factor of the clay-containing stone, resulting in in-plane crack formation. If swelling clays such as montmorillonite are present in a stone, contact with water (e.g., rain event) can cause expansion and scaling of the outermost wet layer in contact with the dry bulk stone underneath. The expanded layer will be under compression, and a buckling phenomenon can develop²⁵. If a flaw of a critical length L is developed parallel to the surface at a depth t , it can trigger buckling along a plane parallel to the exposed surface undergoing expansion. Following Wrangler et al.²⁵ (see Supplementary Note 1) L values of 14.5–87.1 mm are calculated here considering the average $\epsilon = 0.0039$, and the smallest and largest thickness of Copan stone scales, ~ 0.5 –3 mm (determined in thin sections, as well as measuring scales that fell off the stone surfaces at Copan). These L values match scale lengths observed at Copan (Fig. 1f and Supplementary Fig. 1f–g). According to Wrangler et al.²⁵, a flaw propagation mechanism should exist involving microcracks opening until a critical flaw size of the order of magnitude calculated above is reached. Microcracks within

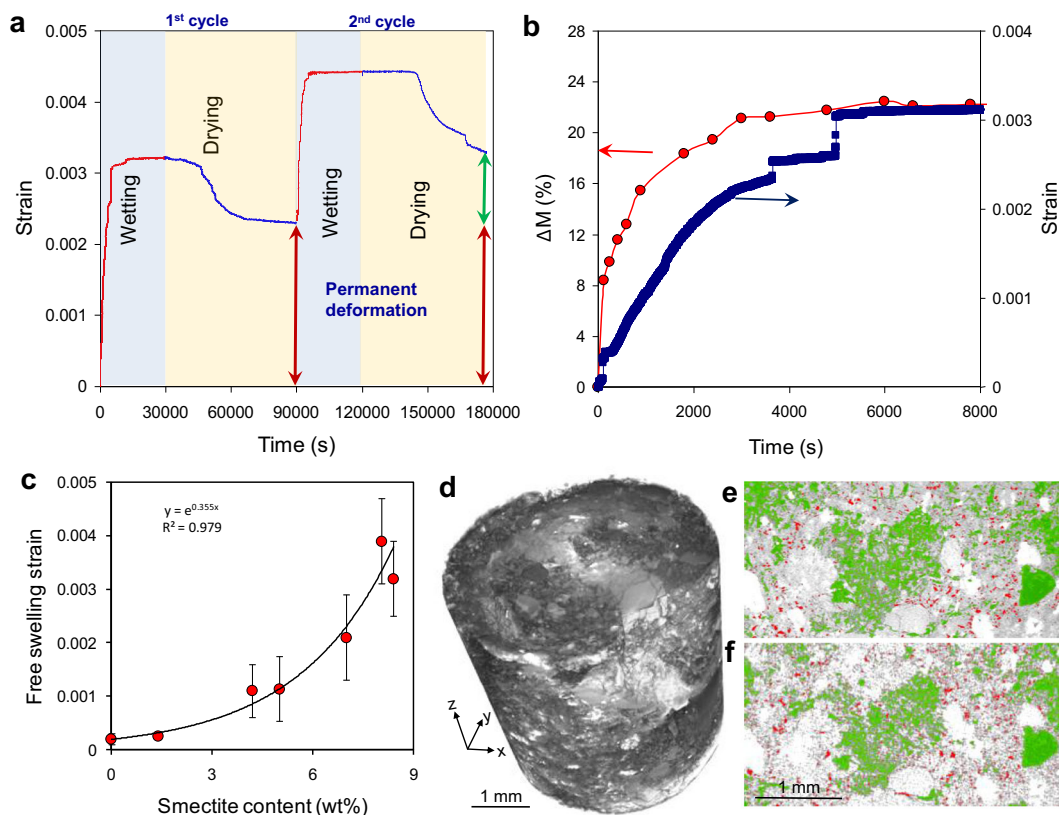


Fig. 3 Hydric expansion of Copan tuff stone (Type 2). **a** Free swelling strain during two wetting/drying cycles. Note the residual strain after the first cycle marked by the red arrow and its increase after the second cycle marked by the green arrow (up to a final residual strain of 0.0033). **b** Time evolution of the water absorption and free swelling strain. **c** Variation of free swelling strain with smectite content (error bars represent stdev, $N = 3$). **d** 3D μ -CT image of Copan stone; 2D section of the stone sample in **(d)** before **(e)** and after **(f)** water saturation. The green and red colors mark the areas of connected and non-connected porosity, respectively.

mineral grains and/or at grain boundaries in Copan stone most likely opened and propagated during the initial stages of scaling damage via clay swelling. This is consistent with the observed residual strain in stone blocks subjected to hydric expansion tests in the laboratory. Upon successive wetting/drying cycles, microcracks would propagate and coalesce, eventually leading to the formation of flaws of critical length L , thus enabling buckling. The latter phenomenon would ultimately lead to the scaling and material loss observed on site. It is very likely that both microbial bioweathering²³ and salt damage (i.e., gypsum crystallization)¹, also contribute to the development of flaws that propagate upon expansion of swelling clays in Copan stone.

It could be argued that expansion/shrinking of zeolites upon wetting/drying of Copan stone could also contribute to the observed strain and associated damage, as has been suggested for the case of other tuff stones²⁶. Although clinoptilolite reportedly undergoes a contraction of the unit cell volume of up to 8% upon dehydration, most zeolites show unit cell volume changes of <2%, and these values are only observed following full dehydration under vacuum at relatively high T ($\geq 200^\circ\text{C}$)²⁷, conditions that are not relevant for stone monuments. Nonetheless, Bish and Carey²⁸ reported volume changes of $\sim 1\%$ at room T for clinoptilolite following changes in relative humidity (RH) from 0–100%, and wetting, conditions that could be relevant for the case of Copan stone damage. To test whether or not zeolites in Copan stone could experience volume expansion during wetting, we performed detailed powder XRD analyses of Type 2 and 3 stones including clinoptilolite, analcime, and mordenite, and subjected to (i) oven drying (60°C , 48 h) and (ii)

wetting (immersion in DI water for 48 h) (see Methods). In the last case, XRD analyses were performed using the wet powders. Our XRD results (Supplementary Fig. 6a–c) show no or negligible shifts in d -spacings of zeolite phases when comparing the Bragg peaks of the dry and wet samples. Only in the case of Type 2 stone with mordenite we observed a slight shift to lower 2θ angles of a few Bragg peaks after wetting (Supplementary Fig. 6c). However, the shift accounted for an increase in d -spacing of up to 0.0047 \AA (for the 640 Bragg peak, which is about 0.2% increase in length along the [640] direction and can be considered negligible). Furthermore, we obtained unit cell volumes of 2737.02 \AA^3 and 2740.13 \AA^3 for the dry and wet mordenite, respectively: i.e., a 0.11% unit cell volume expansion. Such an expansion is basically negligible, particularly if compared with the shift in the 001 Bragg peak of montmorillonite from $\sim 15 \text{ \AA}$ (dry conditions) to $\sim 19.5 \text{ \AA}$ (wet conditions) (Supplementary Fig. 6), corresponding to a $\sim 30\%$ increase in the unit cell volume of this swelling clay. Although our results suggest that zeolite swelling does not seem to be a relevant contributor to the observed hydric strain, its possible (yet limited) contribution to Copan stone swelling damage cannot be fully ruled out.

Altogether, these results provide additional support to the hypothesis that clay swelling is the main mechanism of damage affecting Copan tuff stone, explaining why past treatments with alkoxysilanes failed, as these consolidants crack and lose bonding capacity after a few wetting/drying cycles in clay-containing stones^{4,21}. They also show that for a conservation treatment to be effective, it not only has to strengthen Copan stone acting as a consolidant, but it has also to inhibit clay expansion.

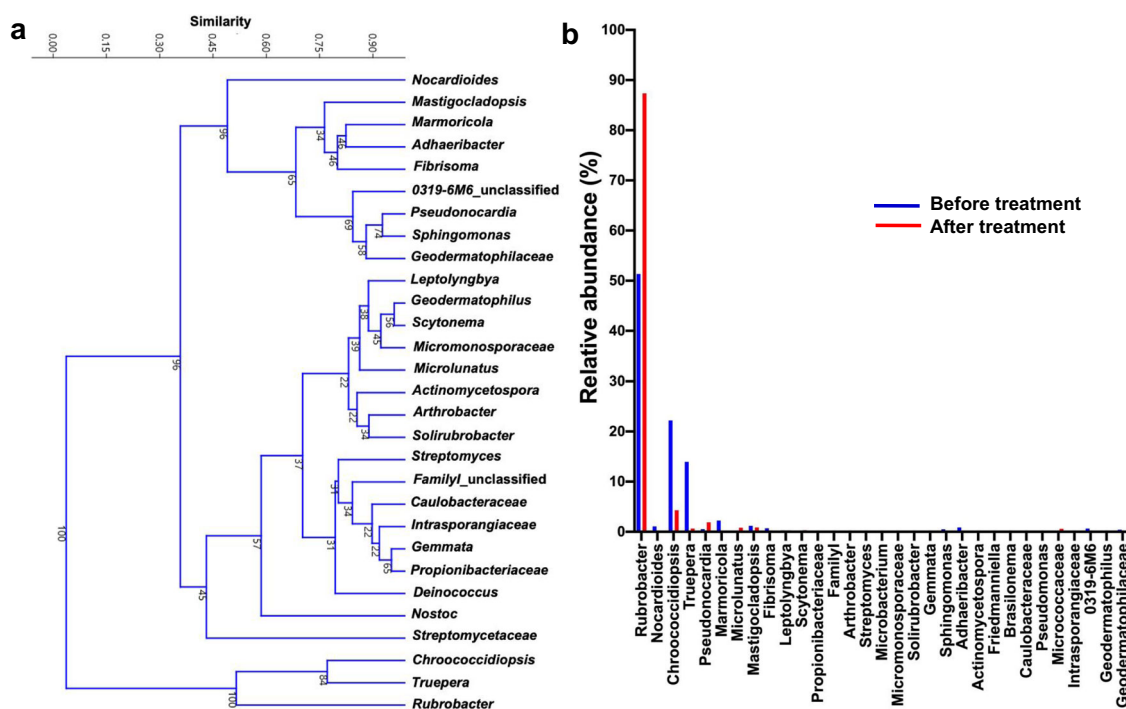


Fig. 4 Analysis of the bacterial community in Copan stone at Structure 10L-18. **a** Phylogenetic tree of identified bacteria. **b** Variation of relative abundance of bacterial species after bacterial treatment.

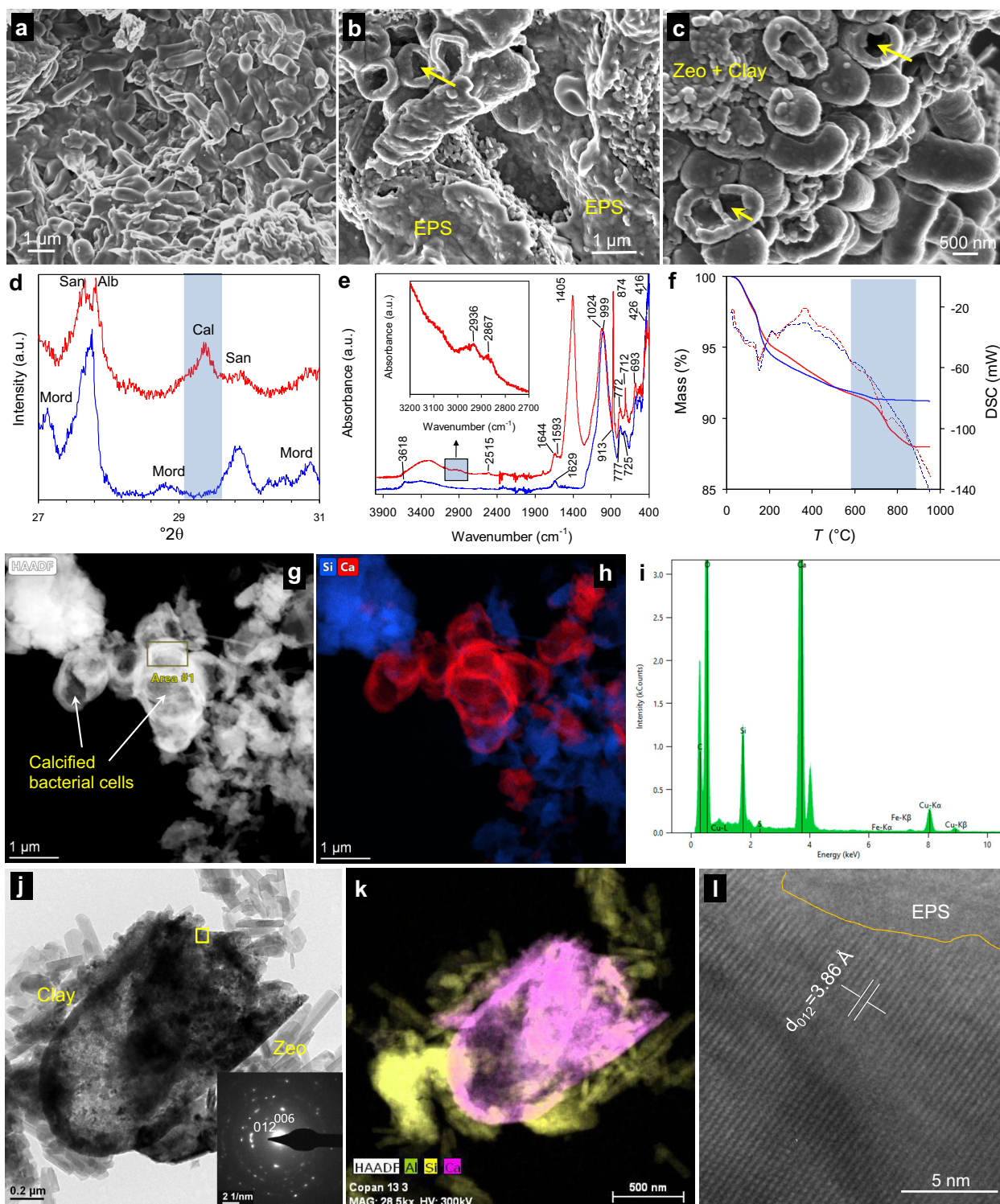
Evolution of stone microbiota after the bioconservation treatment

Our previous genomic analyses demonstrated that tuff stones at Copan originally contained a wide variety of bacterial phyla, with *Actinobacteria* being predominant, followed by *Firmicutes*, *Proteobacteria*, and *Cyanobacteria*²⁹, all commonly present in stone substrates²⁰. An even more marked diversity is observed at the genus level, with *Rubrobacter*, *Chroococcidiopsis*, and *Truepera*, being the dominant genera in untreated Copan tuff stone at Structure 10L-18 (Fig. 4a). After in situ treatment application, a significant increase in *Actinobacteria* was observed. This is an indication of the efficacy of this biotreatment since *Actinobacteria* are known to be able to utilize various carbon and nitrogen sources and produce CaCO_3 ³⁰. In particular, we observed a significant increase in *Rubrobacter* abundance (Fig. 4b). These bacteria have also been detected in stone at the Maya ruins of Uxmal (Mexico)³¹ and are able to tolerate desiccation periods and strong insulation, explaining their abundance at the stone wall of Structure 10L-18. They have been associated with pinkish/reddish discoloration of stone³² and potential salt damage associated with struvite ($\text{NH}_4\text{MgPO}_4 \cdot 6\text{H}_2\text{O}$) precipitation³³. However, none of these phenomena were observed in our samples after in situ and ex situ treatments. Color measurements (Supplementary Table 2) show that values of total color change, ΔE after treatment in the laboratory (see Methods) ranged from 2.6 ± 0.7 for the abundant green variety up to 8.8 ± 0.4 for the buff-greenish variety. The latter ΔE value slightly higher than 5 (a commonly accepted threshold for conservation treatments)¹⁴ was due to a slight increase in lightness, L^* and a small reduction in the $+b^*$ (yellow) component. It is a minor drawback considering the significant color variation displayed by the Copan stones on-site (Fig. 1e and Supplementary Fig. 1), and determined quantitatively for the untreated stone varieties tested in the laboratory ($\Delta E = 7 \pm 4$). The absence of *Rubrobacter*-related pinkish discoloration (which would imply an increase in the $+a^*$ (red) component) is consistent with the fact that light irradiation during treatment was prevented by covering the substrate with a cardboard/plastic. Moreover, no

struvite was detected, likely because M-3P does not include an Mg source.

We observed that all bacteria isolated from the untreated and treated stone blocks and cultured in M-3P medium were carbonatogenic (i.e., they all produced abundant calcite). *Rubrobacter* being carbonatogenic³⁴ and the most abundant bacteria before and after treatment, they likely were the main contributor to CaCO_3 biomineralization within Copan stones (see below). Note that the M-3P nutritional solution selectively activates carbonatogenic bacteria because it contains a pancreatic digest of casein that enables the oxidative deamination of amino acids by such heterotrophic bacteria, generating NH_3 (plus CO_2) and resulting in the alkalization of the medium, ultimately favoring the precipitation of CaCO_3 as the nutritional solution also includes a calcium (acetate) source¹⁴. Moreover, acetate in M-3P is an additional carbon and energy source for heterotrophic carbonatogenic bacteria, contributing to carbonate mineralization via the overall reaction: $2\text{Ca}^{2+} + 2\text{CH}_3\text{COO}^- + 3\text{O}_2 \rightarrow 2\text{CaCO}_3 + 2\text{CO}_2 + 2\text{H}^+$ ³⁵. More importantly, M-3P lacks carbohydrate carbon sources that could induce the activation of deleterious acid-producing bacteria^{11,14}, which were absent in the treated stones.

The total number of culturable bacteria increased from $8.9 \pm 0.9 \times 10^3$ Colony Forming Units (CFU) g^{-1} before treatment to $2.2 \pm 0.2 \times 10^7$ CFU g^{-1} after in situ treatment and from $2.5 \pm 0.5 \times 10^3$ CFU g^{-1} up to $1.2 \pm 0.2 \times 10^7$ CFU g^{-1} after ex situ treatment demonstrating the effectiveness of the treatment. These CFU values are of the same order of magnitude as those observed in porous limestone before and 3 months after successful M-3P treatment at San Jeronimo Monastery in Granada¹⁴. This suggests that the activated bacterial load is not dependent on the substrate lithology (tuff vs. limestone) or the environment (tropical vs. temperate Mediterranean climate). It should be noted that our previous studies showed that the bacterial load returns to pre-treatment values 1 y after treatment¹⁴, which is consistent with our previous results indicating that activated bacteria are entombed in newly formed calcium carbonate and stop proliferating after full consumption of the nutritional solution^{10,14}.



Overall, these results show that Copan stones included an abundant indigenous carbonatogenic bacterial population that was effectively activated following the application of the sterile M-3P nutritional broth. The activated bacteria are typically found in stone structures and monuments throughout the world^{14,29}. Importantly, this treatment also induced a reduction of deleterious acid-producing microbiota in Copan's lime plasters and tuff stone²⁹, which is considered responsible for the observed bioweathering of feldspars (see above). Considering that competition, not cooperation, dominates interactions among microbial species³⁶, by effectively

using the N and C sources in the M-3P culture medium, the indigenous carbonatogenic bacteria proliferated by outcompeting other bacteria using other metabolic routes.

Structural and mineralogical changes upon bacterial treatment

FESEM-EDS analyses showed the proliferation of carbonatogenic bacteria forming bacterial mats on the treated stone surface (Fig. 5a), as well as bacterial CaCO_3 cement embedded in abundant EPS

Fig. 5 Textural and mineralogical characterization of treated Copan stone. **a** FESEM image of bacterial cells developed upon in situ treatment, not yet fully calcified. **b** FESEM image of fully calcified bacterial cells, some with an empty core (arrow), tightly attached to silicates in stone treated in situ. Note the presence of biofilm (EPS) covering the substrate's silicate minerals. **c** Detail of calcified bacterial cells attached to the stone matrix (clays and zeolites; Zeo) after ex situ (laboratory) treatment. Note that calcified structures display a hollow core (i.e., space formerly occupied by the bacterial cells; arrows). **d** XRD patterns of stone before (blue pattern) and after in situ treatment (red pattern) showing bacterial calcite (Cal; 104 Bragg reflection underlined by the shaded area). Other phases present are sanidine (San), albite (Alb), and mordenite (Mord). **e** FTIR spectra of Copan stone before (blue spectrum) and after ex situ bacterial treatment (red spectrum). Inset shows an enlarged view of the C-H stretching region -shaded square-. **f** TG/DSC traces of Copan stone before (blue traces) and after in situ treatment (red traces). The shaded area corresponds to the thermal decomposition of CaCO_3 forming CaO and releasing CO_2 . **g** HAADF image of bacteria cells (bc) with a thin carbonate layer. **h** Ca and Si elemental map of image (g). **i** EDS spectrum of area 1 in the image (g); **j** TEM image of a broken calcified bacterial cell, showing a dark contrast envelope. The SAED pattern (inset) shows that the dark contrast phase is calcite (with preferred orientation along the [100] zone axis). **k** Elemental map of structures shown in (j). **l** HRTEM image of the outer edge of the calcified bacterial cell in (j) (yellow squared area) showing an amorphous layer (upper right), presumably EPS.

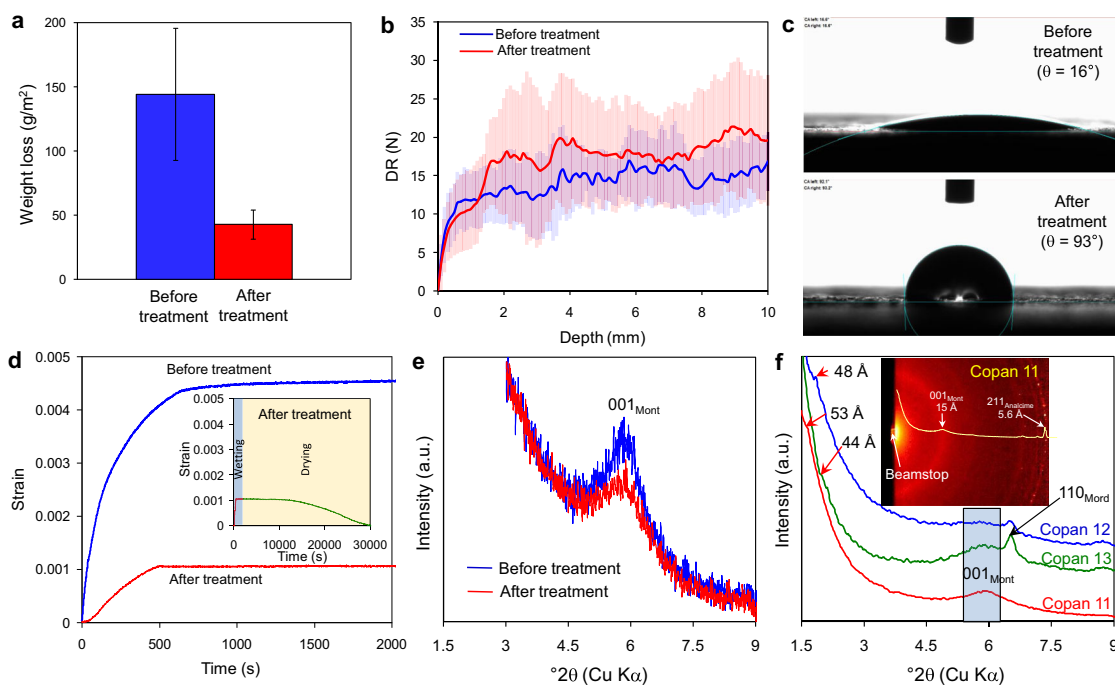


Fig. 6 Evaluation of the treatment's performance. **a** Results of the peeling tape test before and 3 months after in situ treatment. Average values ($N = 12$) and standard deviations are represented. **b** Drilling resistance (DR) along a depth profile of Copan stone before and 3 months after ex situ treatment. Average DR values ($N = 9$) and standard deviations (shaded areas) are represented. **c** Representative examples of water contact angle of Copan stone before and after bacterial treatment. **d** Free swelling strain of Copan stone (Type 3) upon immersion in water. A reduction in maximum strain is observed after bacterial treatment. The inset shows a full wetting/drying cycle of the treated Copan stone. Note the absence of residual strains after complete drying. **e** Conventional XRD pattern of untreated and bacterially treated Copan stone showing a reduction in the intensity of the 001 Bragg peak of montmorillonite (Mont). **f** Small-angle XRD patterns of treated Copan stones (samples Copan 11–13). The red arrows point to peaks and shoulders at d -spacings of 45–53 Å. The blue-shaded area shows the broad 001 Bragg peak of montmorillonite (Mont). The 110 Bragg peak of mordenite (Mord) is indicated. The inset shows the 2D diffraction pattern of sample Copan 11, including the radially integrated line pattern.

within the stone pores (Fig. 5b, c and Supplementary Fig. 7a–b). Abundant pseudospherical and rod-like calcified structures, showing a hollow core corresponding to the former bacterial cell body (Fig. 5b, c), were observed, which cemented the silicate phases without plugging the pores (Supplementary Fig. 7c), as confirmed by MIP measurements (see below). These textural and structural features were observed regardless of whether the treatment was applied in situ or ex situ. FESEM-EDS mapping of sections normal to the surface of stone blocks treated in situ showed Ca-rich precipitates corresponding to calcified bacteria covering the pore walls (not plugging the pores) down to a depth of ~ 7 mm (Supplementary Fig. 8). Such a penetration value is within the range of those reported for low-viscosity alkoxysilane consolidants applied to stones with porosities similar to that of Copan stone³⁷. XRD analysis showed that the newly formed

cement was made up of calcite (Fig. 5d). Before bacterial treatment, Fourier transforms infrared spectroscopy (FTIR) analysis (Fig. 5e) showed the Si-O and Al-O stretching and bending bands of silicate phases (clays, quartz, feldspars, and zeolites) at 999, 913, 777, 725, 693, and 416 cm^{-1} , and the broad ν -OH stretching centered around 3350 cm^{-1} , with a shoulder at 3618 cm^{-1} , and the δ -OH bending at 1629 cm^{-1} of OH and water in montmorillonite³⁸. After treatment, the ν_3 (1405 cm^{-1}), ν_2 (874 cm^{-1}), and ν_4 (712 cm^{-1}) bands of calcite appeared. New bands at 2963 and 2867 cm^{-1} corresponding to the C-H stretching of organics (EPS and bacterial cell debris), as well as a band at 1593 cm^{-1} corresponding to the N-H bending and C-N stretching (amide II) of proteins (blue-shifted from the standard 1554 cm^{-1}), along with broadband centered at ~ 3300 cm^{-1} associated with the amide A band of proteins³⁹ also appeared. These results prove

that EPS, which includes polysaccharides and proteins, with nucleic acids and lipids as minor components⁴⁰, was abundantly produced due to bacterial activation. Upon treatment, the δ -OH bending band blue-shifted from 1629–1644 cm^{-1} and broadened due to the contribution of the amide I band, and the Si-O stretching shifted from 999–1024 cm^{-1} , whereas the shoulder at 913 cm^{-1} corresponding to the Al-OH deformation of smectites disappeared, likely due to its blue-shift and masking by the broad Si-O band at 1024 cm^{-1} . All these changes in band position show that H-bonding was established between EPS and silicates, especially hydroxyl groups of smectites, in accordance with prior findings regarding the interaction of EPS with montmorillonite³⁹. Thermogravimetric/differential scanning calorimetry (TG/DSC) analyses of untreated and treated Copan stone show a weight loss at $T < 550^\circ\text{C}$ largely corresponding to the desorption of adsorbed H_2O and the dehydroxylation of phyllosilicates (Fig. 5f). Additionally, a marked weight loss at $T > 550^\circ\text{C}$ due to the decarbonation of CaCO_3 was observed in the treated stone, corresponding to 7 wt% newly formed bacterial calcite. We also observed a small exothermic peak at 370 $^\circ\text{C}$ in the treated stone, consistent with the combustion of organic matter (EPS and cell debris). TEM-HAADF images (Fig. 5g, h and Supplementary Fig. 9) and EDS analyses (Fig. 5i) show that the bacterial cells were enclosed in a CaCO_3 shell that also cemented the silicate phases. Figure 5j shows a TEM image of a bacterial CaCO_3 shell, calcite according to its selected area electron diffraction (SAED) pattern, consistent with the elemental mapping shown in Fig. 5k. The calcified cells were in close contact with clays (montmorillonite) and zeolite crystals, indicating that the newly formed carbonate cemented such silicate minerals. Figure 5l shows a representative HRTEM image of the external surface of the calcified cell, where calcite lattice fringes abruptly transition to an amorphous phase, presumably EPS.

Altogether, these analyses demonstrate that the abundant bacteria activated with the M-3P solution contributed to the precipitation of significant amounts of calcite in close association with their cell envelope, thereby being encapsulated by the carbonate cement. Such a newly formed cement included organics (EPS). Moreover, the calcified bacterial cells were attached to the silicate substrate, contributing to its cementation as demonstrated below.

Consolidation and protection effects of the biotreatment

The surface consolidation effect of the treatment applied in situ, at Structure 10L-18, was evaluated by the *peeling* test (see Methods). The amount of surface material loss was reduced by $\sim 70\%$ after treatment (Fig. 6a). A more precise evaluation of the strengthening produced by the bacterial treatment applied ex situ was performed using a drilling resistance (DR) measurement system, which enables the evaluation of the effectiveness of a consolidation treatment along a depth profile normal to the treated surface (see Methods). An increase in DR was observed upon treatment, specially marked along the first 3–7 mm of the depth profile (Fig. 6b and Supplementary Fig. 10). In the case of Type 2 stone blocks (Fig. 6b) the increase in DR spanned along the full 10 mm depth profile, pointing to the deep penetration of the treatment. The increase in average DR along the depth profiles ranged from 4% in Type 3 stone up to 24% in Type 2 stone. Such a substantial in-depth strengthening is due to two effects: (i) the newly formed carbonate cement binds the silicate minerals and partly fills pores/cracks as shown by FESEM analyses (Fig. 5b, c and Supplementary Fig. 7c), thus reducing both the density/length of flaws that could result in fracture propagation, and the stone's porosity, increasing its strength. The latter effect is, however, limited because the porosity reduction is $< 8.5\%$, with minimal changes in the pore size distribution, according to MIP results (Supplementary Fig. 11); and (ii) the newly formed bacterial CaCO_3 is a biomineral, that is, a

hybrid material made up of calcite including organic products (EPS) of bacterial activity^{10,14,41}, having superior mechanical properties (hardness and toughness) than inorganic calcite, as shown for other CaCO_3 biominerals such as mollusk shells⁴². Indeed, bacterial calcite shows a nanoindentation hardness of up to $3.92 \pm 0.43 \text{ GPa}$ ⁴³, a value 57% higher than that of geologic calcite ($\sim 2.5 \text{ GPa}$)⁴⁴. It might be argued that the DR increase could be in part due to the precipitation of calcium phosphate phases⁴⁵, as M-3P includes 10 mM phosphate buffer, and its solid residue after complete desiccation is made up of hydroxylapatite¹⁰. However, we did not detect any calcium phosphate phase(s) after treatment. Similarly, we can rule out possible cementation associated with the abiotic precipitation of CaCO_3 based on our previous tests showing that application of sterile M-3P to sterile carbonate and silicate substrates does not result in CaCO_3 precipitation⁴⁶.

To disclose if the bacterial treatment also had a protective effect, we performed static contact angle measurements and studied changes in the kinetics of water droplets absorption on Copan stone prior to and after in situ and ex situ treatment (see Methods). We observed a large increase in contact angle from ~ 0 – 30° ($15 \pm 12^\circ$, $N = 11$) up to 93° ($66 \pm 27^\circ$, $N = 4$) before and after in situ treatment, respectively (Fig. 6c). Laboratory stone blocks showed values of $5 \pm 0.5^\circ$ ($N = 53$) before treatment and up to 90° ($66 \pm 15^\circ$, $N = 40$) after treatment. The low values observed before treatment are due to the hydrophilic silicate nature of the tuff stone, being in the same range as those of silicate minerals such as quartz ($0^\circ < \theta < 40^\circ$)⁴⁷. As a result, the 4 μL water droplets used to measure the contact angle were absorbed within $5 \pm 2 \text{ s}$ ($N = 3$) once deposited on the untreated Copan stone, whereas it took $163 \pm 39 \text{ s}$ ($N = 9$) for their absorption on the treated substrates. These results show that the bacterial biofilm (bacterial cells + EPS) formed on the pore walls of Copan stone after treatment imparted hydrophobicity to the substrate. This is in agreement with previous results showing that topography and specific components of polysaccharides and proteins in EPS impart a significant hydrophobicity to bacterial biofilms⁴⁸. These effects have profound implications in the protection of the treated Copan stone, as water is demonstrated here to be the main contributor to its physical weathering. Hydric expansion tests of treated Copan stone (Fig. 6d) showed that as compared with untreated stone samples: (i) the free swelling strain curves showed a delayed start and slower kinetics; (ii) the maximum ε was reduced by a factor of up to 4.5 (e.g., from 0.0045–0.001; Fig. 6d), and (iii) no residual strain was observed after completing successive wetting/drying cycles. The change in swelling kinetics is consistent with the observed kinetics of water droplet suction associated with the hydrophobic character of the biofilm covering the stone pore walls. Changes in swelling behavior suggest that carbonatogenic bacterial biofilms, and EPS in particular, prevent/limit smectite swelling during wetting, hindering crack opening and propagation (i.e., resulting in buckling, see above) and, thus, permanent deformation upon drying. These effects previously unknown for bacterial treatments are of extremely high relevance for the protection of Copan stones. They show that the treatment not only contributes to the in-depth strengthening of the stone (i.e., consolidation effect) but also tackles the main cause of decay (i.e., protection effect), which is demonstrated here to be clay swelling. By acting on the root of the decay problem, the treatment will limit future damage.

We hypothesize that this protection effect is related to the interaction of bacterial-derived organics (i.e., EPS) with montmorillonite. It is known that several organic (macro)molecules can be adsorbed in the interlayer of smectites, thus modifying their interaction with water. For instance, protonated dialkylammonium ions have been shown to substitute interlayer cations in swelling clays, thereby reducing interlayer (crystalline) hydration and acting as swelling inhibitors when applied to clay-rich stones^{18,22}.

Incorporation of organics, including EPS, into the interlayer of smectites is commonly detected by a change (normally, an increase) in the d_{001} -spacing⁴⁹. However, our results using conventional XRD showed no changes in d_{001} -spacing of montmorillonite after treatment, but a decrease in the intensity of the broad 001 Bragg peak (Fig. 6e). A possible effect of the interaction of montmorillonite with polymers is the delamination of crystallites and their dispersion within the polymer continuum, resulting in an intensity decrease or even disappearance of the 001 reflections, consequently drastically limiting crystalline swelling⁵⁰. Alternatively, polymers might be incorporated within smectite clays forming an intercalated structure with either a non-periodic or a periodic arrangement (large d -spacing, not detected by our conventional XRD with a cut-off at $3^\circ 2\theta$), which can also result in the reduction of the intensity of 001 Bragg peaks⁵⁰. Importantly, small-angle XRD analysis (see Methods) of treated Copan stones showed small peaks and shoulders at $2\theta < 2^\circ$ corresponding to d -spacings of 44–53 Å (Fig. 6f). Similar values have been observed following intercalation of DNA between montmorillonite layers, resulting in swelling inhibition despite the fact that a 001 peak (with reduced intensity) remained at the original d_{001} -spacing of this phase⁵¹, as in our case. Our small-angle XRD results and the observed reduction in the intensity of the 001 Bragg peak suggest that intercalation of EPS within montmorillonite occurred in treated Copan stones. Intercalation most likely involved H-bonding between functional groups of EPS (e.g., amide groups) and water/OH molecules of montmorillonite, which is consistent with our FTIR results (see above). Additionally, bridging of the clay particles by EPS polymer strands could also aid in the stabilization of the clay structure against swelling, as observed in the case of soil clays in contact with EPS and/or organic matter⁵². It is therefore very likely that the observed reduction in hydric expansion and the absence of residual strain upon wetting/drying tests in bacterially treated Copan stones are due to the combined effects of EPS-clay interactions and cementation associated with the newly formed bacterial CaCO_3 . It should be noted that while biofilms, and EPS in particular, have been associated with biodeterioration of stone² and bioweathering of silicate minerals^{53,54}, there is mounting evidence that microbial biofilms can actually have a protective effect against physical and chemical weathering of building stone^{55,56}.

In summary, our results demonstrate that the main mechanism of decay of Copan tuff stone is physical in nature, and caused by expansion and contraction (swelling-shrinking) of smectitic clays (montmorillonite) present in significant concentrations in the stone lithotypes most prone to decay. Repeated wetting (and drying) induces crack formation and propagation, resulting in buckling of the wet surface layers of the stone, a massive formation of scales, and material loss, as observed in the archaeological site. Microbial bioweathering of Copan stone minerals, feldspars in particular, appears to contribute to the weakening of the tuff stone, facilitating the development of critical flaws and the progress of clay swelling-related damage. Past conservation interventions involving the application of conventional consolidation treatments have failed mainly because they did not tackle the primary decay mechanism. Our approach for the conservation of these invaluable carved Classic Maya tuff stone structures and sculptures involving the application of a sterile nutritional solution (M-3P), which selectively activates the abundant indigenous carbonatogenic bacteria identified in the stone, bypasses the limitations of previous conventional conservation treatments. It results in an effective consolidation of the treated porous stone because it induces the formation of bacterial calcite cement. Moreover, the activated carbonatogenic bacteria produce abundant EPS, which imparts hydrorepellency to the stone substrate and, what is more important, drastically reduces the free swelling strain of the stone. This will prevent future spalling and scaling damage. These results also suggest that the

extended practice involving the elimination of microbial biofilms, for instance using biocides (e.g., Clorox, as occurred in Copan decades ago), should be reconsidered as some biofilms (e.g., those including no deleterious acid-producing bacteria) may contribute to the protection of the substrate.

Overall, our study demonstrates that from both, a microbiological and a conservation point of view, this biotreatment is highly effective at protecting and consolidating heavily damaged clay-containing tuff stones, and produces no known side effects. Remarkably, the effectiveness of this treatment is very high despite the fact that it has been applied in a non-carbonate tuff stone and in a tropical environment. This and the fact that the identified carbonatogenic bacterial species in the stone's indigenous microbial community are among the most common in stone artworks and monuments all over the world, including clay-containing stones (not solely tuff but also limestones and sandstones), ensures that this easy to apply, and highly effective bio-conservation method might have widespread application not only in the Maya area, but elsewhere. Nonetheless, we want to stress that prior to application of this bacterial treatment in other Maya sites, or elsewhere, extensive research on its effectiveness (and potential limitations), including both laboratories and in situ pilot testing, should be performed. It would also be necessary to evaluate the treatment performance over the long-term (years), as it is planned for the pilot test area in Copan.

METHODS

Selection and analysis of weathered Copan stone

Samples of Copan stone ($N = 13$) were collected in different areas of the archaeological site to have a representative pool of stone material (considering different weathering patterns and compositional/textural heterogeneity) for analysis, as well as for testing and evaluation of the bacterial bioconservation treatment. Supplementary Fig. 1h shows the samples' location and their description. In particular, detailed sampling was performed in a selected area of Structure 10L-18 (Fig. 1e), the last construction of the so-called Copan Principal Group, which includes the Copan Acropolis (ca. 805 CE). The area was chosen because it showed advanced deterioration through scaling and flaking, leading to crumbling and loss of surface stone material (Fig. 1f and Supplementary Fig. 1f–g). The sampled area in Structure 10L-18 was selected for the in situ trial application of the bacterial conservation biotreatment, whereas samples Copan 11 to 13 (Supplementary Fig. 1h) were subjected to bacterial biotreatment ex situ (in the laboratory) (see details below). Sampling was performed prior to, and 3 months after treatment. Stone textural features were studied on a polarized light petrographic microscope (Olympus V) with transmitted and reflected light, using uncovered polished thin sections. The mineralogy was determined by XRD on a PANalytical X'Pert Pro equipped with Ni filter (measurement parameters: Cu K α radiation $\lambda = 1.5405 \text{ \AA}$, 45 kV, 40 mA, 3 to $70^\circ 2\theta$ exploration range, steps of $0.001^\circ 2\theta$, and goniometer speed of $0.01^\circ 2\theta \text{ s}^{-1}$). Powder samples were deposited on zero-background Si sample holders for analysis. Mineral phases were identified by comparison with JCPDS (Joint Committee on Powder Diffraction Standards) powder spectra using the X'Pert computer program⁵⁷ and quantified using the Rietveld method⁵⁸ with internal crystalline silicon standard for quantification of amorphous phases -i.e., volcanic glass- using the X'Pert Pro software (PANalytical). The clay fraction ($< 2 \mu\text{m}$) was separated via differential sedimentation after grinding and dispersion in water. Oriented aggregates were prepared (air-dried, ethylene glycol (EG) solvated at 60°C for 48 h, dimethyl sulfoxide (DMSO) solvated for 48 h at 60°C , and heat-treated for 1 h at 550°C) and analyzed by XRD. The bulk chemical composition of Copan stone samples was determined by X-ray fluorescence analysis (FRX) on a PANalytical Zetium. TG-DSC (Mettler-Toledo TGA/DSC1) was used to determine the amount of carbonates formed after bacterial consolidation. Solids were also analyzed by ATR-FTIR (Jasco) in the spectral range $4000\text{--}400 \text{ cm}^{-1}$ with a step size of 0.48 cm^{-1} . Additional microstructural features of untreated and treated Copan stone samples were determined by FESEM (Zeiss AURIGA) equipped with EDS microanalysis. Samples were carbon-coated prior to FESEM observations. Ultrastructural features and detailed chemistry of mineral phases of the untreated and treated samples were studied using TEM on a Titan and a Talos (FEI) with an acceleration voltage of 300 and 200 kV,

respectively. Both TEMs are equipped with HAADF detector for Z-contrast imaging and EDS for microanalysis. Analytical electron microscopy (AEM) was performed in scanning TEM (STEM) mode using the thin foil method⁵⁹ and experimental *k*-factors determined for each TEM using standard mineral phases.

The hydric expansion of the untreated and treated stone samples was measured using in-house equipment. Prior to testing, stone blocks (~2 × 2 × 3 cm in size) were first oven-dried (48 h at 60 °C), and later on left to equilibrate with the laboratory conditions (19 ± 1 °C, 41 ± 2% RH) for at least 24 h. The testing device included a linear variable displacement transducer (LVDT, with ± 1 μm accuracy) fixed to a clamp, in contact with the upper surface of the tested stone blocks, which in turn were placed in a crystallization dish. Afterwards, DI water was added until the water level reached the top of the stone block while the linear expansion was continuously measured. Once the signal stabilized at a maximum expansion value, the water in the crystallization dish was evacuated using a pipette. LVDT measurements were also collected during drying until a constant value was reached (after complete drying). A second wetting-drying cycle was performed while collecting LVDT data. In parallel, the water absorption of the stone blocks was evaluated by immersion in DI water, measuring the stone samples mass change over time using a balance. Upon saturation, the stone blocks were subjected to forced saturation under vacuum for 24 h and the water-accessible porosity was calculated according to the Archimedes principle⁶⁰.

The possible expansion of Copan stone upon wetting associated with changes in unit cell volume of zeolites was studied using XRD. Prior to XRD analysis, powder samples of Type 2 and 3 stones including clinoptilolite (Copan-2), analcime (Copan-11), and mordenite (Copan-12) were subjected to (i) oven drying at 60 °C for 48 h, and (ii) wetting, achieved by immersion in DI water for 48 h at room *T*. In the last case, the XRD analysis was performed using the wet powder. Samples were spiked with silicon powder (the internal standard used for accurate *d*-spacing measurements). Shifts in Bragg peaks position following wetting were only detected in the case of samples containing mordenite. To evaluate the expansion underwent by this zeolite, we refined its unit cell parameters using the X Powder computer program⁵⁷ and the mordenite structure data in JCPDS file # 83-1676.

The textural/structural changes undergone by the Copan stone following contact with water were studied in situ at high magnification by high-resolution Micro-CT (Versa Xradia 510, Zeiss) equipped with a custom-made fluid cell. Scans were performed at 60 kV and 83 mA. Data were acquired with a 4x magnification charge-coupled device (CCD) objective for a total scan time of up to 8 h including the collection of reference images, with an exposure time of 5 s and a source-sample distance of 35 mm and a detector-sample distance of 15 mm. The voxel size achieved under these conditions was 4.8 μm. A cylindrical piece of Type 2 Copan stone (~4 mm in diameter and ~10 mm in length) was introduced into the fluid cell and several scans were collected both before and after water flooding (for a duration of up to 8 h). Image analysis was performed to quantify total, communicated, and occluded porosity using the Dragonfly software (Version 4.1, Object Research Systems).

Bacterial conservation biotreatment

Two tuff stone blocks showing similar extensive deterioration in Structure 10L-18 were selected for the in situ trial application of our bacterial bioconsolidation treatments (Fig. 1e). Additionally, parallelepipeds (~2 × 2 × 3 cm) were cut from three stone blocks (corresponding to samples Copan 11 -Type 3-, and Copan 12 and 13 - Type 2-) with differing degrees of deterioration (from negligible to advanced) that were aseptically collected at the bottom of Structure 10L-22 and Structure 10L-16 of the Copan Acropolis (Supplementary Fig. 1h) and transported in hermetically sealed plastic bags to our laboratories in Granada (Spain). Such samples were treated ex situ, in the laboratory. The treatment consisted in the application of a sterile M-3P nutritive solution [1 wt % Bacto Casitone, 1 wt% Ca(CH₃COO)₂·4H₂O, 0.2 wt% K₂CO₃·1/2 H₂O in a 10 mM phosphate buffer, pH 8] without the addition of any microorganism. The treatment (both in situ and ex situ) was applied by spray (until stone saturation) twice a day (to avoid desiccation) on six consecutive days. The total amount of M-3P solution applied was approximately 0.2 mL cm⁻². To maintain the stone adequately damp and protected from direct light irradiation (to avoid possible bacterial pigmentation), the areas treated in situ (as well as laboratory treated stone blocks) were covered with cardboard/black plastic foil (not in direct contact with the stone surface) during the treatment and up to three days after treatment completion (i.e., until the solutions

evaporated completely). The treatment application is described in further detail in Jroundi et al.¹⁴.

Our nutritive medium is specifically designed to activate the carbonatogenic bacteria present in stones. Moreover, it does not include any carbohydrate, which might lead to the activation and proliferation of acid-producing deleterious bacteria. Note that Copan (Honduras) is located on the southeastern frontier of the Maya Lowland culture area (latitude, 14° 51' 30" N, longitude, 89° 9' W)⁶¹. With an elevation of ~700 m a.s.l. and an average annual *T* of ~26 °C with precipitation averaging ~2000-3000 mm annually⁶², the site is subjected to hot and humid tropical conditions. Treatments were performed in situ in mid-February, the end of the dry season in Copan, when the average maximum and minimum *T* in the area are 29 °C and 16 °C, respectively, and the RH is ~80 ± 5%, conditions highly favorable for bacterial proliferation after the activation with the nutritive broth. Similar *T* and RH conditions were maintained in the laboratory during treatment.

Molecular identification of the bacterial community

Samples were collected at Structure 10L-18 from one stone block before and after treatment under sterile conditions using tweezers and transferred to sterile Eppendorf tubes, which were immediately sealed and only opened later on for analysis. Genomic DNA was extracted, and high-throughput amplicon sequencing using 250 bp paired-end sequencing (MiSeq Illumina) was performed. Total DNA of each sample was amplified targeting the hypervariable V3-V4 regions by using the 16 S rRNA gene primers 341 F and 785R⁶³. Illumina libraries were constructed and sequenced at LGC Genomics, GMBH, Berlin, Germany (<http://www.lgcgroup.com/>). The detailed protocol for DNA extraction and Illumina sequencing, as well as the results of such analysis for the case of several stone and plaster samples from Copan have been published elsewhere²⁹. Here we only report details of the bacterial species identified using such a molecular method in the case of the tuff stone samples collected from Structure 10L-18 before and 3 months after bacterial bioconsolidation treatment.

Evolution of culturable microbiota

The evolution of the culturable microbiota developed after both in situ (Structure 10L-18 at Copan) and ex situ (laboratory) treatment application was tracked prior to and 3 months after treatment. Stone grains from treated and untreated stone blocks (~300 mg per sample) were collected and added to 1 ml of nutritive M-3P solution. Each sample was then gently mixed, and aliquots were collected for serial dilution in sterile 0.9 wt% NaCl solution, from which the total number of bacteria was assessed using TSA culture medium (Scharlau Microbiology, Spain). To determine the carbonatogenic capacity of the members of the bacterial community in the tuff stone, the stone samples collected prior to and after treatment were inoculated on plates of M-3P solid medium (M-3P supplemented with 2% purified agar, DifcoTM) and incubated at 28 °C to obtain colonies. Controls of sterile culture medium were incubated in parallel. Petri dishes were periodically examined by optical microscopy for the presence of calcium carbonate crystals. The carbonatogenic activity was considered high when CaCO₃ precipitates were covering the whole colony and were also present in the bulk medium.

Evaluation of the efficacy of the bacterial treatment

In situ tests at Copan were performed before treatment and 3 months after treatment application. To quantify the change in the surface cohesion after the bio-consolidation treatments, the so-called *peeling* (or *Scotch tape*) test was used⁶⁴. This test, which has been successfully utilized to test the efficacy of stone conservation treatments¹⁴, involves the measurement of the weight difference of adhesive tape pieces (before and after they have been stuck to the stone surface) and calculating the weight of the detached stone material per unit surface area. The adhesive tape removes loose and/or poorly cemented surface stone grains/flakes, therefore, variations in the mass of grains removed by the tape enable quantification of the surface consolidation achieved by the treatment. Pieces of adhesive tapes (7 × 3.5 cm²) were stuck on the stone surface and rapidly removed. This operation was performed on the stone surface, both before and after in situ treatment. To ensure statistical significance, a minimum of 3 replicates per sampled area was performed.

Drilling resistance (DR) was measured before and 3 months after treatment of the stone blocks treated in the laboratory using a drilling resistance measurement system (DRMS; Sint Technology). Due to travel constraints, it was not possible to perform such a test in situ, at the Copan

site. DR measurements enable to evaluate the level of consolidation (strengthening) in-depth profiles⁶⁵. The DRMS continuously measures the force (N) necessary to drill a hole in material under constant rotational speed (ω) and penetration rate (v). We used a 5 mm diameter Diaber drill bit (Sint Technology) with a flat-edged diamond-tip, with v of 10 mm/min and ω of 600 rpm (optimal for porous stones). A calibration standard of known DR was also drilled to ensure no variation in DR associated with the wear of the drill bit tip during the course of the tests.

Changes in the porosity and pore size distribution of Copan stone following the treatment were measured using mercury intrusion porosimetry (Micromeritics, Autopore 9600). Stone pieces (~1 g) from samples collected before and 3 months after treatment application (both in situ and ex situ) were oven-dried for 24 h at 80 °C prior to analysis.

Variation in CIEL*a*b* color parameters after stone treatment in the laboratory were measured using a Minolta Chroma Meter spectrophotometer equipped with Xenon lamp (Illuminant C) and diffuse reflectance geometry. Total color variations are reported here as $\Delta E = (\Delta L^* + \Delta a^* + \Delta b^*)^{1/2}$, where ΔL^* , Δa^* and Δb^* are, respectively, the difference in values between the untreated and treated stone of: L^* (lightness: 0 being black and 100 being diffuse white), a^* (negative values indicate green whilst positive values indicate magenta), and b^* (negative values indicate blue and positive values indicate yellow). To ensure statistical significance, a minimum of 6 color measurements were performed per test area.

The static contact angle of the Copan stone samples before and after treatment (both those collected from Structure 10L-18 and those tested in the laboratory) was measured using the sessile drop (4 μ L DI water) method on a DataPhysics OCA 15EC device equipped with Peltier stage (25 °C) and SCA software. To ensure statistical significance, at least 6 measurements per sample were performed. In parallel, we measured the time necessary for the absorption of each drop as an indication of a hydrophobic protection effect after the treatment.

In addition to standard XRD analysis, we also performed small-angle XRD analysis of the samples subjected to treatment in the laboratory. For this task, we used a Bruker D8 Discover equipped with a Dacris Pilatus3R 100K-A 2D detector and an adjustable (0.1–2 mm beam diameter) X-ray microbeam (Cu K α ; 40 kV and 40 mA). We collected an X-ray scattering signal for $2\theta \geq 1.52^\circ$ (i.e., d -spacing $\leq 58.07 \text{ \AA}$). The X-ray beam diameter was fixed at 0.5 mm and further line collimated using a Z-adjustable slit (knife-edge) placed 10 cm from the beam source. The direct beam contribution to the XRD 2D pattern was minimized by placing at an appropriate height a Z-adjustable beamstop (5 cm apart from the sample, next to the 2D detector). Note that while this setup enables the collection of 1D small-angle X-ray scattering (SAXS) signal, it does not provide data of enough quality to perform a detailed and accurate SAXS analysis. Analyses were performed using bulk powder samples (placed in glass capillaries) and clay oriented aggregates with the following equipment parameters: 1.5–40 $^\circ 2\theta$ explored area, 0.02 $^\circ 2\theta$ step size and integration time of 0.4 s per step.

DATA AVAILABILITY

All data that support the findings of this study are available from the corresponding author upon reasonable request.

Received: 7 May 2021; Accepted: 29 July 2021;

Published online: 17 August 2021

REFERENCES

- Doehne, E. & Price, C. *Stone Conservation: An Overview of Current Research* (The Getty Conservation Institute, 2010).
- Warscheid, T. & Braams, J. Biodeterioration of stone: a review. *Int. Biodeterior. Biodegrad.* **46**, 343–368 (2000).
- McNamara, C. J., Perry, T. D. IV, Bearce, K. A., Hernandez-Duque, G. & Mitchell, R. Epilithic and endolithic bacterial communities in limestone from Maya Archaeological Site. *Microb. Ecol.* **51**, 51–64 (2006).
- Wheeler, G. *Alkoxysilanes and the Consolidation of Stone* (Getty Conservation Institute, Los Angeles, 2005).
- Giorgi, R., Baglioni, M., Berti, D. & Baglioni, P. New methodologies for the conservation of cultural heritage: micellar solutions, microemulsions, and hydroxide nanoparticles. *Acc. Chem. Res.* **43**, 695–704 (2010).
- Fash, W. L., Williamson, R. V., Larios, C. R. & Palka, J. The hieroglyphic stairway and its ancestors: investigations of copan structure 10L-26. *Anc. Mesoam.* **3**, 105–115 (1992).

- Williams, H. & McBirney, A. R. *Volcanic History of Honduras* (University of California Press, Berkeley, 1969).
- The Getty Conservation Institute and Instituto Hondureño de Antropología e Historia, The Hieroglyphic Stairway of Copán, Honduras: Study Results and Conservation Proposals. (The Getty Conservation Institute, Los Angeles, 2006). http://www.getty.edu/conservation/publications_resources/pdf_publications/copan.html.
- Caneva, G., Salvadori, O., Ricci, S. & Ceschin, S. Ecological analysis and biodeterioration processes over time at the Hieroglyphic Stairway in the Copán (Honduras) archaeological site. *Plant Biosyst.* **139**, 295–310 (2005).
- Rodríguez-Navarro, C., Rodríguez-Gallego, M., Chekroun, K. B. & Gonzalez-Munoz, M. T. Conservation of ornamental stone by Myxococcus xanthus-induced carbonate biomineralization. *Appl. Environ. Microbiol.* **69**, 2182–2193 (2003).
- González-Muñoz, M. T., Rodríguez-Navarro, C., Jimenez-Lopez, C. & Rodríguez-Gallego, M. Method and product for protecting and reinforcing construction and ornamental materials. Spanish Patent 2008/009771 (2008).
- De Muynck, W., De Belie, N. & Verstraete, W. Microbial carbonate precipitation in construction materials: a review. *Ecol. Eng.* **36**, 118–136 (2010).
- Rodríguez-Navarro, C., Jroundi, F. & Gonzalez-Muñoz, M. T. Stone consolidation by bacterial carbonatogenesis: evaluation of in situ applications. *Restor. Build. Monum.* **21**, 9–20 (2015).
- Jroundi, F. et al. Protection and consolidation of stone heritage by self-inoculation with indigenous carbonatogenic bacterial communities. *Nat. Commun.* **8**, 279 (2017).
- Rodrigues, J. D. & Pinto, A. P. F. Stone consolidation by biomineralisation. Contribution for a new conceptual and practical approach to consolidate soft decayed limestones. *J. Cult. Herit.* **39**, 82–92 (2019).
- Rodríguez-Navarro, C., Sebastian, E., Doehne, E. & Ginell, W. S. The role of sepiolite-palygorskite in the decay of ancient Egyptian limestone sculptures. *Clays Clay Miner.* **46**, 414–422 (1998).
- Heiken, G. Tuffs - Their Properties, Uses, Hydrology, and Resources (The Geological Society of America, Sp. Paper 408, Boulder, CO, 2006).
- Jiménez-González, I., Rodríguez-Navarro, C. & Scherer, G. W. Role of clay minerals in the physicochemical deterioration of sandstone. *J. Geophys. Res.: Earth Surf.* **113**, F02021 (2008).
- Wangler, T. & Scherer, G. W. Clay swelling mechanism in clay-bearing sandstones. *Environ. Geol.* **56**, 529–534 (2008).
- Wedekind, W., López-Doncel, R., Dohrmann, R., Kocher, M. & Siegesmund, S. Weathering of volcanic tuff rocks caused by moisture expansion. *Environ. Earth Sci.* **69**, 1203–1224 (2013).
- Felix, C. & Furlan, V. Variations dimensionnelles de grès et calcaires, liées à leur consolidation avec un silicate d'éthyle. In *The Conservation of Monuments in the Mediterranean Basin*: Proc. 3rd Int. Symp. (eds. Fassina, V. Ott, H. & Zezza, F.) 855–859 (Soprintendenza ai Beni Artistici e Storici di Venezia, Venice, 1994).
- Wendler, E., Charola, A. E. & Fitzner, B. Easter Island tuff: Laboratory studies for its consolidation. In Proc. 8th Int. Conf. on the Deterioration and Conservation of Stone (ed. Riederer, J.) 1159–1170 (Rathgen-Forschungslabor, Berlin, 1996).
- Rogers, J. R., Bennett, P. C. & Choi, W. J. Feldspars as a source of nutrients for microorganisms. *Am. Mineral.* **83**, 1532–1540 (1998).
- Schult, A. & Shi, G. Hydration swelling of crystalline rocks. *Geophys. J. Int.* **131**, 179–186 (1997).
- Wangler, T. P., Stratulat, A., Duffus, P., Prévost, J. H. & Scherer, G. W. Flaw propagation and buckling in clay-bearing sandstones. *Environ. Earth Sci.* **63**, 1565–1572 (2011).
- Lubelli, B., Nijland, T. G. & Tolboom, H.-J. Moisture induced weathering of volcanic tuffstone. *Constr. Build. Mater.* **187**, 1134–1146 (2018).
- Bish, D. L. & Carey, J. W. Thermal behavior of natural zeolites. *Rev. Mineral. Geochem.* **45**, 403–452 (2001).
- Bish, D. L. & Carey, J. W. Coupled X-ray powder diffraction and thermogravimetric analysis of clinoptilolite dehydration behavior. In *Natural Zeolites for the Third Millennium* (eds. Colella, C. & Mumpton, F. A.) 249–257 (De Frede Editore, Napoli, 2000).
- Jroundi, F., Elert, K., Ruiz-Agudo, E., Gonzalez-Muñoz, M. T. & Rodríguez-Navarro, C. Bacterial diversity evolution in Maya plaster and stone following a bio-conservation treatment. *Front. Microbiol.* **11**, 599144 (2020).
- Fang, B. Z. et al. Insights on the effects of heat pretreatment, pH, and calcium salts on isolation of rare actinobacteria from karstic caves. *Front. Microbiol.* **8**, 1535 (2017).
- Ortega-Morales, B. O., Narváez-Zapata, J. A., Schmalenberger, A., Sosa-López, A. & Tebba, C. C. Biofilms fouling ancient limestone Mayan monuments in Uxmal, Mexico: a cultivation-independent analysis. *Biofilms* **1**, 79–90 (2004).
- Schabereiter-Gurtner, C., Piñar, G., Vybiral, D., Lubitz, W. & Rölleke, S. Rubrobacter related bacteria associated with rosy discolouration of masonry and lime wall paintings. *Arch. Microbiol.* **176**, 347–354 (2001).
- Laiz, L. et al. Isolation of five Rubrobacter strains from biodeteriorated monuments. *Naturwissenschaften* **96**, 71–79 (2009).

34. Pellerin, A., Lacelle, D., Fortin, D., Clark, I. D. & Lauriol, B. Microbial diversity in endostromatolites (cf. fissure calcretes) and in the surrounding permafrost landscape, Haughton impact structure region, Devon Island, Canada. *Astrobiology* **9**, 807–822 (2009).
35. Yoshida, N., Higashimura, E. & Saeki, Y. Catalytic biomineralization of fluorescent calcite by the thermophilic bacterium *Geobacillus thermoglucosidasius*. *Appl. Environ. Microbiol.* **76**, 7322–7327 (2010).
36. Foster, K. R. & Bell, T. Competition, not cooperation, dominates interactions among culturable microbial species. *Curr. Biol.* **22**, 1845–1850 (2012).
37. Leroux, L. et al., Measuring the penetration depth of consolidating products: comparison of six methods. In Proc. 9th Int. Cong. Deterioration and Conservation of Stone (ed. Fassina, V.) 361–369 (Elsevier, Amsterdam, 2000).
38. Madejová, J. FTIR techniques in clay mineral studies. *Vib. Spectrosc.* **31**, 1–10 (2003).
39. Cao, Y. et al. Preferential adsorption of extracellular polymeric substances from bacteria on clay minerals and iron oxide. *Colloids Surf. B* **83**, 122–127 (2011).
40. Flemming, H. C. et al. Biofilms: an emergent form of bacterial life. *Nat. Rev. Microbiol.* **14**, 563–575 (2016).
41. Yin, X. et al. Directing effect of bacterial extracellular polymeric substances (EPS) on calcite organization and EPS–carbonate composite aggregate formation. *Cryst. Growth Des.* **20**, 1467–1484 (2020).
42. Kamat, S., Su, X., Ballarini, R. & Heuer, A. H. Structural basis for the fracture toughness of the shell of the conch *Strombus gigas*. *Nature* **405**, 1036–1040 (2000).
43. Dhama, N. K., Mukherjee, A. & Reddy, M. S. Micrographical, mineralogical and nano-mechanical characterisation of microbial carbonates from urease and carbonic anhydrase producing bacteria. *Ecol. Eng.* **94**, 443–454 (2016).
44. Kim, Y. Y. et al. Tuning hardness in calcite by incorporation of amino acids. *Nat. Mater.* **15**, 903–910 (2016).
45. Sassoni, E., Naidu, S. & Scherer, G. W. The use of hydroxyapatite as a new inorganic consolidant for damaged carbonate stones. *J. Cult. Herit.* **12**, 346–355 (2011).
46. Rodríguez-Navarro, C., Jroundi, F., Schiro, M., Ruiz-Agudo, E. & González-Muñoz, M. T. Influence of substrate mineralogy on bacterial mineralization of calcium carbonate: implications for stone conservation. *Appl. Environ. Microbiol.* **78**, 4017–4029 (2012).
47. Lamb, R. N. & Furlong, D. N. Controlled wettability of quartz surfaces. *J. Chem. Soc., Farad. Trans.* **78**, 61–73 (1982).
48. Epstein, K., Pokroy, B., Seminara, A. & Aizenberg, J. Bacterial biofilm shows persistent resistance to liquid wetting and gas penetration. *Proc. Natl Acad. Sci. USA* **108**, 995–1000 (2011).
49. Alimova, A. et al. Bacteria–clay interaction: structural changes in smectite induced during biofilm formation. *Clays Clay Miner.* **57**, 205–212 (2009).
50. Alexandre, M. & Dubois, P. Polymer-layered silicate nanocomposites: preparation, properties and uses of a new class of materials. *Mater. Sci. Eng. Rep.* **28**, 1–63 (2000).
51. Yamaguchi, N. et al. Swelling inhibition of liquid crystalline colloidal montmorillonite and beidellite clays by DNA. *Sci. Rep.* **8**, 4367 (2018).
52. Chenu, C. Clay—or sand—polysaccharide associations as models for the interface between micro-organisms and soil: water related properties and microstructure. *Geoderma* **56**, 143–156 (1993).
53. Banfield, J. F., Barker, W. W., Welch, S. A. & Taunton, A. Biological impact on mineral dissolution: application of the lichen model to understanding mineral weathering in the rhizosphere. *Proc. Natl Acad. Sci. USA* **96**, 3404–3411 (1999).
54. Barker, W. W., Welch, S. A., Chu, S. & Banfield, J. F. Experimental observations of the effects of bacteria on aluminosilicate weathering. *Am. Mineral.* **83**, 1551–1563 (1998).
55. Pinna, D. Biofilms and lichens on stone monuments: do they damage or protect? *Front. Microbiol.* **5**, 133 (2014).
56. Carter, N. E. A. & Viles, H. A. Bioprotection explored: the story of a little known earth surface process. *Geomorphology* **67**, 273–281 (2005).
57. Martin-Ramos, J. D. X Powder: A software package for powder X Ray diffraction analysis, <http://www.xpowder.com> (2004).
58. Rietveld, H. A profile refinement method for nuclear and magnetic structures. *J. Appl. Crystallogr.* **2**, 65–71 (1969).
59. Cliff, G. & Lorimer, G. The quantitative analysis of thin specimens. *J. Microsc.* **103**, 203–207 (1975).
60. RILEM 25-PEM, Recommended tests to measure the deterioration of stone and to assess the effectiveness of treatment methods. *Mater. Struct.* **13**, 175–253 (1980).
61. Webster, D. The archaeology of Copan, Honduras. *J. Archaeol. Res.* **7**, 1–53 (1999).
62. McVey, L. A Characterization and Analysis of the Floor Plasters from the Acropolis at Copan, Honduras. Ms Thesis. University of Pennsylvania, Philadelphia, PA (1998).
63. Klindworth, A. et al. Evaluation of general 16S ribosomal RNA gene PCR primers for classical and next-generation sequencing-based diversity studies. *Nucleic Acids Res.* **41**, e1 (2013).
64. Dráčky, M. et al. Standardization of peeling tests for assessing the cohesion and consolidation characteristics of historic stone surfaces. *Mater. Struct.* **45**, 505–520 (2012).
65. Pamplona, M., Kocher, M., Sneathlage, R. & Aires Barros, L. Drilling resistance: overview and outlook. *Z. dt. Ges. Geowiss.* **158**, 665–676 (2007).

ACKNOWLEDGEMENTS

We acknowledge funding by the Santander Program for the Research and Conservation of Maya Sculpture, at the David Rockefeller Center for Latin American Studies (DRCLAS), Harvard University; the Spanish Government grant RTI2018-099565-B-I00, the Junta de Andalucía research groups RNM-179 and BIO 103, and the University of Granada, Unidad Científica de Excelencia UCE-PP2016-05. We thank the Instituto Hondureño de Antropología e Historia (IHAA) and the local Santander team at the Maya Sculpture Conservation Laboratory (LACEM) in Copan including Hector Eliud Guerra, Karina Garcia, Adolfo Canan, Rufino Membreño, Luis Reina, and Isuara Nereyda Alonso for their help and continuous support, as well as for providing access to this Maya archaeological site and their contribution to the documentation, sampling, and treatment application process. We also thank architectural conservator Laura Lacombe for sampling support, Fulvio di Lorenzo for his help with Rietveld analysis of XRD results, George W. Scherer for his insightful comments on clay swelling damage, and the personnel of the Centro de Instrumentación Científica (CIC) of the University of Granada for their help with TG/DSC, XRD, FRX, μ -CT, FESEM and TEM analyses. We also thank Aurelia Ibañez Velasco for her help with the expansion tests, as well as with the porosity and water absorption analyses, and Jean Battini from Micromeritics France S.A.R.L., for the MIP analyses.

AUTHOR CONTRIBUTIONS

CRN and KE conceived and designed the project; CRN, BWF, WLF, NV, and ADT coordinated and performed sampling and field tests; MTGM and FJ performed the microbiological analysis; KE, CRN, and ERA performed laboratory tests and analysis, and contributed to the interpretation of results along with contributions by all authors; CRN and KE wrote the manuscript with contributions by all authors.

COMPETING INTERESTS

The authors declare no competing interests.

ADDITIONAL INFORMATION

Supplementary information The online version contains supplementary material available at <https://doi.org/10.1038/s41529-021-00191-4>.

Correspondence and requests for materials should be addressed to C.R.-N.

Reprints and permission information is available at <http://www.nature.com/reprints>

Publisher's note Springer Nature remains neutral with regard to jurisdictional claims in published maps and institutional affiliations.



Open Access This article is licensed under a Creative Commons Attribution 4.0 International License, which permits use, sharing, adaptation, distribution and reproduction in any medium or format, as long as you give appropriate credit to the original author(s) and the source, provide a link to the Creative Commons license, and indicate if changes were made. The images or other third party material in this article are included in the article's Creative Commons license, unless indicated otherwise in a credit line to the material. If material is not included in the article's Creative Commons license and your intended use is not permitted by statutory regulation or exceeds the permitted use, you will need to obtain permission directly from the copyright holder. To view a copy of this license, visit <http://creativecommons.org/licenses/by/4.0/>.

© The Author(s) 2021